

3D Universal Lesion Detection and Tagging in CT with Self-Training

Jared Frazier¹, Tejas Sudharshan Mathai¹, Jianfei Liu¹,
Angshuman Paul², and Ronald M. Summers¹

¹Imaging Biomarkers and Computer-Aided Diagnosis Laboratory, Radiology and Imaging
Sciences, Clinical Center, National Institutes of Health, Bethesda MD, USA

²Indian Institute of Technology, Jodhpur, Rajasthan, India

ABSTRACT

Radiologists routinely perform the tedious task of lesion localization, classification, and size measurement in computed tomography (CT) studies. Universal lesion detection and tagging (ULDT) can simultaneously help alleviate the cumbersome nature of lesion measurement and enable tumor burden assessment. Previous ULDT approaches utilize the publicly available DeepLesion dataset, however it does not provide the full volumetric (3D) extent of lesions and also displays a severe class imbalance. In this work, we propose a self-training pipeline to detect 3D lesions and tag them according to the body part they occur in. We used a significantly limited 30% subset of DeepLesion to train a VFNet model for 2D lesion detection and tagging. Next, the 2D lesion context was expanded into 3D, and the mined 3D lesion proposals were integrated back into the baseline training data in order to retrain the model over multiple rounds. Through the self-training procedure, our VFNet model learned from its own predictions, detected lesions in 3D, and tagged them. Our results indicated that our VFNet model achieved an average sensitivity of 46.9% at [0.125:8] false positives (FP) with a limited 30% data subset in comparison to the 46.8% of an existing approach that used the entire DeepLesion dataset. To our knowledge, we are the first to jointly detect lesions in 3D and tag them according to the body part label.

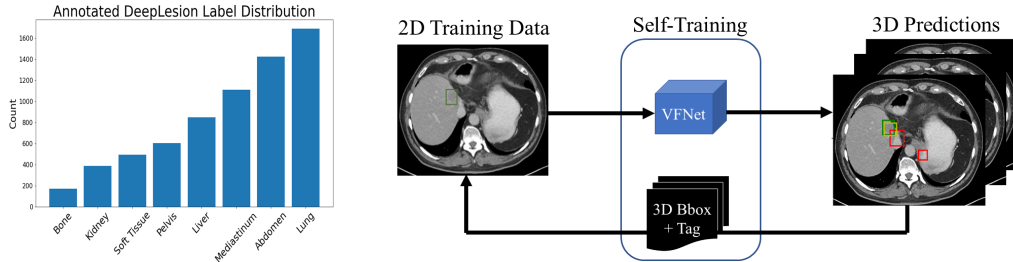
Keywords: CT, Lesion, Neural Networks, Detection, Classification, 3D Context, Self-Training

1. INTRODUCTION

Radiologists routinely size lesions in patient CT studies to estimate tumor burden and stage cancer.¹⁻³ They scroll through the volumetric slices to find the lesion extent, but prospectively measure the lesion size on a single slice to determine malignancy^{2,4,5} according to RECIST guidelines.¹ However, this guideline varies across institutions due to many factors, such as clinical practice, type of CT scanners, exam protocols, contrast phases used. Moreover, the RECIST measurements do not indicate the true 3D lesion extent with regions of the same lesion instance in adjoining slices remaining unmarked.⁴⁻⁶ As the 3D lesion extent can be a potential indicator of response to treatment, it is crucial to detect and label the 3D lesions, such that their size can be accurately measured based on current guidelines. Prior approaches^{3-5,7-14} for 3D lesion detection used the publicly available DeepLesion dataset,⁷ but it contains incomplete annotations^{5,6,15} and severe class imbalances.^{6,15}

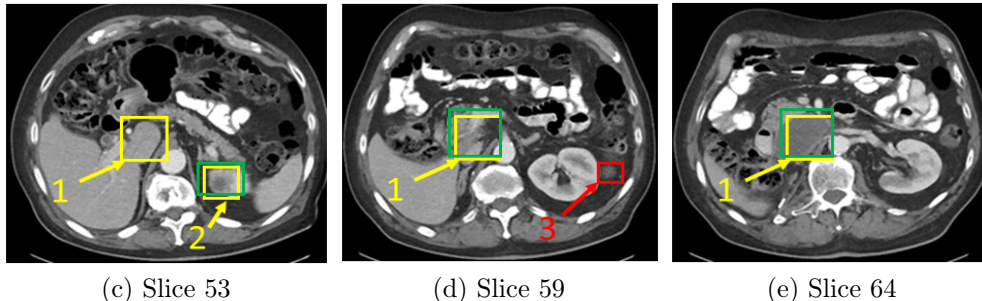
In this work, we designed a self-training pipeline for 3D lesion detection and tagging. We used a limited 30% data subset of DeepLesion consisting of lesion bounding boxes and coarse body part labels to train a VFNet model¹⁶ for 2D lesion detection and tagging. Our model subsequently expanded the context of the 2D boxes + tags in the training set to 3D, and also mapped the 2D boxes + tags predicted on an unseen DeepLesion training set into 3D. These 3D lesion predictions were integrated back into the training data when the confidence scores exceeded a certain threshold to ensure robustness against noise. Self-training was done over multiple rounds, and the proposed model effectively learned from its own predictions and re-trained itself for 3D lesion detection and tagging. Finally, an ensemble of the best performing models across the self-training rounds was used for 3D lesion detection and tagging on a held-out test set.

Send correspondence to T.S.M.: tejas dot mathai at nih dot gov



(a) Label distribution of the DeepLesion

(b) Self-training pipeline



(c) Slice 53

(d) Slice 59

(e) Slice 64

Figure 1: (a) Distribution of lesion labels in the DeepLesion validation + test splits showing class imbalances. (b) Proposed self-training pipeline. A VFNet model was trained on 2D lesions annotations from the baseline training split, and it iteratively mined new 2D predictions on the training data and on an unseen data split (original DeepLesion training split). Following this step, the 2D predictions were consolidated based on IoU overlap and expanded into 3D. Next, the 3D predictions were incorporated into the baseline training split for re-training the model over multiple rounds. (c) - (e) 3D predictions with confidence score $\geq 50\%$ shown for different slices of an abdominal CT volume. They were generated by the ensemble of models from different mining rounds self-trained with the variable threshold policy. Green: Ground Truth, Yellow: True Positive ($\text{IoU}^5 \geq 30\%$), and Red: False Positive. Lesion 1 is a GT “abdomen” lesion spanning across slices [58, 73], while the predicted 3D proposal spans slices [53, 73]. Despite GT boxes being absent for lesion 1 in slices 53 through 57, the 3D proposal has an $\text{IoU}^5 \geq 30\%$ with the GT and is considered a TP. Notice that lesion 1 is visible across all displayed slices. Lesion 2 is a GT “kidney” lesion spanning slices [52, 57] with the predicted 3D lesion spanning slices [53, 54]. Lesion 3 is a predicted 3D “abdomen” lesion spanning slices [59, 63], and it was counted as a FP during lesion detection + tagging. This lesion was not annotated in the official DeepLesion test split, and thus the tag from this split was not mapped to the fully annotated LENS test split (see Sec. 2 for details). Therefore, it is *not* a FP with respect to detection only. Also, the correct tag for lesion 3 is a “kidney” cyst, but these lesion types are often confused with the “liver” and “abdomen” classes. It is not visible in slice 64 due to the predicted extent.

2. METHODS

Data. The DeepLesion dataset⁷ has 10,594 CT studies from 4,427 patients with 32,120 CT slices containing 32,735 lesions annotated with 2D bounding boxes. It was divided into official training (70%), validation (15%) and testing (15%) splits with the lesions in the validation and testing splits tagged with one of 8 coarse body part tags (bone, abdomen, mediastinum, liver, lung, kidney, soft tissue, pelvis). As we aim to achieve ULDT in this work, we use only the validation and testing splits (30% of total data). The official training split was used for lesion mining and all the annotations were discarded. To generate a 3D test set, we used the LENS⁵ test split, which contained 1000 sub-volumes randomly drawn from the DeepLesion test split with all lesions in each sub-volume fully annotated with 3D bounding boxes. Note that these 3D bounding boxes were not tagged, and we mapped the tags from the 2D lesion annotations in the official DeepLesion test split to the 3D boxes in LENS test split when the intersection over union (IoU) between them exceeded 10%. This meant that the 2D annotation in DeepLesion test split corresponded to the same 3D annotation in the LENS test split. After the labels were mapped, any patients in the official test split that overlapped with the 3D LENS test split were removed to prevent data leakage. A summary of the limited dataset we used is shown in Table 1.

Table 1: Summary of label distributions for the limited 30% DeepLesion dataset used in this study.

Subset	Bone	Abdomen	Mediastinum	Liver	Lung	Kidney	Soft tissue	Pelvis	Total
Train	97	788	613	426	1039	195	288	321	3767
Val	44	318	258	205	345	82	107	189	1548
Test	31	319	239	217	308	109	99	94	1416
Total	172	1425	1110	848	1692	386	494	604	6731

3D Lesion Detection and Tagging. A recently proposed object detector called Varifocal Net¹⁶ (VFNet) was used for ULDT. VFNet was trained to predict a lesion’s 2D bounding box and body part label in a CT slice. Weighted Boxes Fusion¹⁷ (WBF) was used to consolidate the numerous predictions from multiple epochs of a single model or from multiple models. If the IoU between the predicted 2D boxes across multiple consecutive slices exceeded 30%,⁵ they were consolidated together to generate the 3D context for a predicted lesion. In this way, the 3D lesion prediction was made up of a cluster of 2D boxes. The $[x, y]$ coordinates of the final 3D bounding box were computed as the average of the 2D boxes weighted by their detection scores. The body part tag for the 3D lesion prediction was obtained from the tag of the constituent 2D box with the highest predicted confidence. Implementation details followed that prior work³ and details are described in Sec. 5.1.

Self-Training with Intra- and Inter-Patient Data. VFNet was used to iteratively mine new 3D lesions in *our* baseline train split (intra-patient) and the *official* DeepLesion training split (inter-patient). Mined 3D lesions that were predicted in these splits were filtered based on exceeding a specified confidence score (see Sec. 3). These 3D mined lesions were incorporated back into the baseline training split, and the model was re-trained (from scratch) on some of its own predictions. The self-training procedure was repeated for four mining rounds.

3. EXPERIMENTS AND RESULTS

Experimental Design. Two different 3D lesion mining experiments were conducted for incorporating lesion proposals back into the baseline training split. The first experiment E_S used a static threshold to include 3D lesion predictions with confidence scores $\geq 80\%$ across the mining rounds. The static threshold was selected under the belief that high quality lesions would be mined that lead to an efficient lesion detector. The second experiment E_V varied the confidence score threshold across mining rounds. An initial threshold of 80% was set for the first round and it was progressively lowered by 10% across remaining rounds. E_V operated under the belief that larger lesion quantities would be mined across rounds to improve detection performance. An additional facet of both experiments was the upsampling of mined 3D proposals in the baseline training set, such that an approximately even distribution of each lesion type was visible to the model during training. First, the number of predicted lesions for the most predominant class in a round was computed, and then the number of lesions of all other classes were upsampled to match that of the prevalent class. The lesion upsampling strategy was adopted because a disproportionate number of mined 3D proposals could further exacerbate the class imbalance in the DeepLesion dataset as seen in Fig. 1(a). It would also nullify the need to discard mined 3D lesions across over-represented classes in order to balance them against the under-represented classes. We compared these experimental results against those from a model that underwent no self-training. Consistent with prior work,^{4,5} we present our results of sensitivity at 4 FP/volume, sensitivity at [0.125,0.25,0.5,1,2,4,8] FP/volume, and at 30% intersection of bounding box (IoBB) overlap⁴ on the LENS test split in Table 2 and Fig. 1.

Results and Discussion. The VFNet model without self-training achieved a mean sensitivity of 46.7% at [0.125:8] FP/vol with the highest sensitivities for over-represented classes (abdomen 72.4%) and the lowest sensitivities seen for under-represented classes (kidney 61.5%, pelvis 61.7%). Comparing the static threshold experiment E_S against the model with no self-training, the sensitivity at [0.125:8] FP/vol was slightly lower (46.7% vs 46.5%). It became evident that only 3/8 classes (kidney, abdomen, and soft tissue) maintained or improved the sensitivity with self-training at 4FP/vol. We believe the “Abdomen” class performed poorly because the original DeepLesion dataset⁷ described this class as a “catch-all” term for all abdominal lesions that were not “Kidney” or “Liver” masses. However, these two organs are in close proximity to each other anatomically, and axial slices often show cross-sections of both the liver and kidney in the same slice as seen in Fig. 1(c). The

Table 2: 3D lesion detection and tagging performance of VFNet. Sensitivities were calculated at 4FP and at 30% IOBB⁵ overlap. Averaged sensitivity at [0.125, 0.25, 0.5, 1, 2, 4, 8] FP is also shown.

Round	Bone	Kidney	Soft Tissue	Pelvis	Liver	Mediastinum	Abdomen	Lung	Sens@0.125:8FP
No Self-Training (Baseline)									
Round 0	77.4	61.7	72.7	61.5	68.2	61.9	72.4	48.6	46.7
# Lesions used	97 (2.6%)	195 (5.2%)	288 (7.6%)	321 (8.5%)	426 (11.3%)	613 (16.8%)	788 (20.9%)	1039 (27.6%)	-
E_S – Static Threshold Policy [80%, 80%, 80%, 80%]									
Round 1 (80%)	64.5	56.4	76.8	54.1	66.4	56.5	69.5	48.0	44.8
Round 2 (80%)	64.5	58.5	77.8	54.1	69.1	56.9	68.8	50.2	44.8
Round 3 (80%)	67.7	50.0	71.7	54.1	65.4	64.0	67.9	48.6	43.1
Round 4 (80%)	74.2	45.7	67.8	61.5	62.2	54.4	66.6	44.5	42.2
Ensemble of Rounds	71.0	59.6	72.7	62.4	65.9	57.7	71.1	51.4	46.5
# Lesions mined	279 (4.3%)	245 (3.7%)	256 (3.9%)	71 (1.1%)	756 (11.5%)	1084 (16.5%)	3347 (51.0%)	521 (8.0%)	-
E_V – Variable Threshold Policy [80%, 70%, 60%, 50%]									
Round 1 (80%)	64.5	56.4	76.8	54.1	66.4	56.5	69.5	48.0	44.8
Round 2 (70%)	77.4	54.3	75.8	56.0	63.6	55.2	71.1	46.7	43.9
Round 3 (60%)	64.5	50.0	73.7	57.8	65.4	56.5	65.9	42.6	42.1
Round 4 (50%)	67.7	59.6	67.8	54.1	65.0	54.0	67.2	38.9	40.8
Ensemble of Rounds	77.4	58.5	75.7	61.5	68.2	56.9	70.1	43.0	46.9
# Lesions mined	1494 (2.6%)	3849 (6.6%)	3850 (6.6%)	1070 (1.8%)	7577 (12.9%)	7455 (12.7%)	26009 (44.5%)	7169 (12.3%)	-

confusion matrices shown in Figs. 2, 3, and 4 confirmed this belief as it showed that the “abdomen” lesions were predominantly confused with the “liver” masses and “kidney” lesions.

Comparing the variable threshold experiment E_V against the model without self-training, we noticed that the average sensitivity at [0.125:8] FP/vol was higher (46.9% vs 46.7%). Amongst the under-represented classes (bone, kidney, soft tissue, pelvis), 3/4 classes maintained or improved their performance. Only the “kidney” class showed a $\sim 3\%$ drop in sensitivity at 4FP. Among the over-represented classes, we observed that only 1/4 classes (liver) maintained or improved their detection performance with self-training. The remaining classes saw a small decrease in sensitivity at 4FP. The model from E_V performed similarly when compared against the results described in prior work⁵ on the same test dataset (46.9% vs 46.8%). Specifically, we show similar performance with a *significantly* smaller dataset (30% of original DeepLesion) in contrast to prior work⁵ who used the entire DeepLesion dataset in conjunction with models trained on additional datasets^{18–20} for lesion mining.

4. CONCLUSIONS

In this work, we developed a self-training pipeline for 3D universal lesion detection and tagging. We used only a 30% fraction of the DeepLesion dataset to train a VFNet model for 2D ULDT. Following this, the model simultaneously expanded the 2D boxes and tags into 3D for the training split and an unseen data split (official DeepLesion training split). The 3D proposals were then incorporated into the baseline training data when the confidence scores of the proposals exceeded a confidence threshold. Self-training ensued with the model learning from its own predictions over multiple rounds. The final trained model was used for evaluation, and predicted 3D lesions and their tags for a separate test split. We have shown that our average sensitivity of 46.9% at [0.125:8] FP/vol is comparable to 46.8% of prior work⁵ where the entire DeepLesion dataset was used.

ACKNOWLEDGMENTS

This work was supported by the Intramural Research Program of the NIH Clinical Center.

REFERENCES

- [1] Schwartz, L. and et al., “Recist 1.1—update and clarification: From the recist committee,” *European Journal of Cancer* **62**, 132–137 (2016).
- [2] McNitt-Gray, M. F., Kim, G. H., Zhao, B., Schwartz, L. H., Clunie, D., Cohen, K., Petrick, N., Fenimore, C., Lu, Z. J., Buckler, A. J., and et al., “Determining the variability of lesion size measurements from ct patient data sets acquired under “no change” conditions,” *Translational Oncology* **8**(1), 55–64 (2015).
- [3] Mattikalli, T., Mathai, T. S., and Summers, R. M., “Universal lesion detection in CT scans using neural network ensembles,” in [*Medical Imaging 2022: Computer-Aided Diagnosis*], Drukker, K., Iftekharuddin, K. M., Lu, H., Mazurowski, M. A., Muramatsu, C., and Samala, R. K., eds., **12033**, 878 – 882, International Society for Optics and Photonics, SPIE (2022).
- [4] Cai, J., Harrison, A. P., Zheng, Y., Yan, K., Huo, Y., Xiao, J., Yang, L., and Lu, L., “Lesion-harvester: Iteratively mining unlabeled lesions and hard-negative examples at scale,” *IEEE Transactions on Medical Imaging* **40**(1), 59–70 (2021).
- [5] Yan, K., Cai, J., Zheng, Y., Harrison, A. P., Jin, D., Tang, Y., Tang, Y., Huang, L., Xiao, J., and Lu, L., “Learning from multiple datasets with heterogeneous and partial labels for universal lesion detection in ct,” *IEEE Transactions on Medical Imaging* **40**(10), 2759–2770 (2021).
- [6] Naga, V., Mathai, T. S., Paul, A., and Summers, R. M., “Universal lesion detection and classification using limited data and weakly-supervised self-training,” arXiv (2022).
- [7] Yan, K. and et al., “DeepLesion: automated mining of large-scale lesion annotations and universal lesion detection with deep learning,” *Journal of Medical Imaging* **5**(3), 1 – 11 (2018).
- [8] Yang, J., He, Y., Huang, X., Xu, J., Ye, X., Tao, G., and Ni, B., “Alignshift: Bridging the gap of imaging thickness in 3d anisotropic volumes,” in [*Medical Image Computing and Computer Assisted Intervention – MICCAI 2020*], Martel, A. L., Abolmaesumi, P., Stoyanov, D., Mateus, D., Zuluaga, M. A., Zhou, S. K., Racoceanu, D., and Joskowicz, L., eds., 562–572, Springer International Publishing, Cham (2020).
- [9] Tang, Y. and et al., “ULDOR: a universal lesion detector for ct scans with pseudo masks and hard negative example mining,” in [*ISBI*], 321–329 (2019).
- [10] Xie, C. and et al., “Recist-net: Lesion detection via grouping keypoints on recist-based annotation,” in [*ISBI*], 921–924 (2021).
- [11] Zlocha, M. and et al., “Improving retinanet for ct lesion detection with dense masks from weak recist labels,” in [*MICCAI*], (2019).
- [12] Yan, K. and et al., “3d context enhanced region-based convolutional neural network for end-to-end lesion detection,” in [*MICCAI 2018*], 511–519 (2018).
- [13] Yang, J., He, Y., Kuang, K., Lin, Z., Pfister, H., and Ni, B., “Asymmetric 3d context fusion for universal lesion detection,” in [*Medical Image Computing and Computer Assisted Intervention – MICCAI 2021*], de Bruijne, M., Cattin, P. C., Cotin, S., Padoy, N., Speidel, S., Zheng, Y., and Essert, C., eds., 571–580, Springer International Publishing, Cham (2021).
- [14] Li, H., Chen, L., Han, H., and Zhou, S. K., “Satr: Slice attention with transformer for universal lesion detection,” arXiv (2022).
- [15] Erickson, P. D., Mathai, T. S., and Summers, R. M., “Class imbalance correction for improved universal lesion detection and tagging in ct,” arXiv (2022).
- [16] Zhang, H. and et al., “Varifocalnet: An iou-aware dense object detector,” in [*CVPR*], (2021).
- [17] Solovyev, R. and et al., “Weighted boxes fusion: Ensembling boxes from different object detection models,” *Image and Vision Computing* **107**, 104117 (2021).
- [18] Setio, A. and et al., “Validation, comparison, and combination of algorithms for automatic detection of pulmonary nodules in computed tomography images: The luna16 challenge,” in [*Medical Image Analysis*], **42**, 1–13 (2017).
- [19] Bilic, P. and et al., “The liver tumor segmentation benchmark (lits),” arXiv (2019).
- [20] Roth, H. R. and et al., “A new 2.5d representation for lymph node detection using random sets of deep convolutional neural network observations,” in [*Medical Image Computing and Computer-Assisted Intervention – MICCAI 2014*], 520–527, Springer International Publishing, Cham (2014).

5. SUPPLEMENTARY MATERIAL

5.1 Implementation

The window center and width (e.g. [-175,275]) values provided in the DeepLesion dataset were used to window the Hounsfield units (HU) in a CT slice and clip them to the [0,255] range. Additionally, slices above and below the annotated slice were also windowed and normalized. To mimic the radiologist’s approach of scrolling through slices in a CT volume, we constructed a 2.5D image with three consecutive slices (middle slice was the annotated slice) for training the detectors. Each slice was resized to 512×512 pixels dimension before being fed to the detectors. The backbone network for VFNet was a ResNet-50 model, and data was augmented through standard strategies, such as random flipping, rotation, intensity shifts, crops. The batch size was set to 2, the learning rate was $1e^{-3}$, and VFNet was trained for 16 epochs. Experiments were run on a workstation running Ubuntu 18.04 LTS with 4 Tesla V100 GPUs. Fusion of predictions through WBF was done at test time with the top 5 epochs having the lowest validation for each model type with the exception of the ensemble of self-trained models. For the ensemble of self-trained models, the epoch having the lowest validation loss for each self-trained model was used for fusion of 2D predictions. Consistent with literature, models were evaluated at 0.30 IOBB threshold.⁵ The IOBB threshold is computed by calculating the intersection of predicted bounding boxes and ground truth bounding boxes and then dividing by the area of the predicted bounding boxes (as implemented in the [github](#) of prior work⁵).

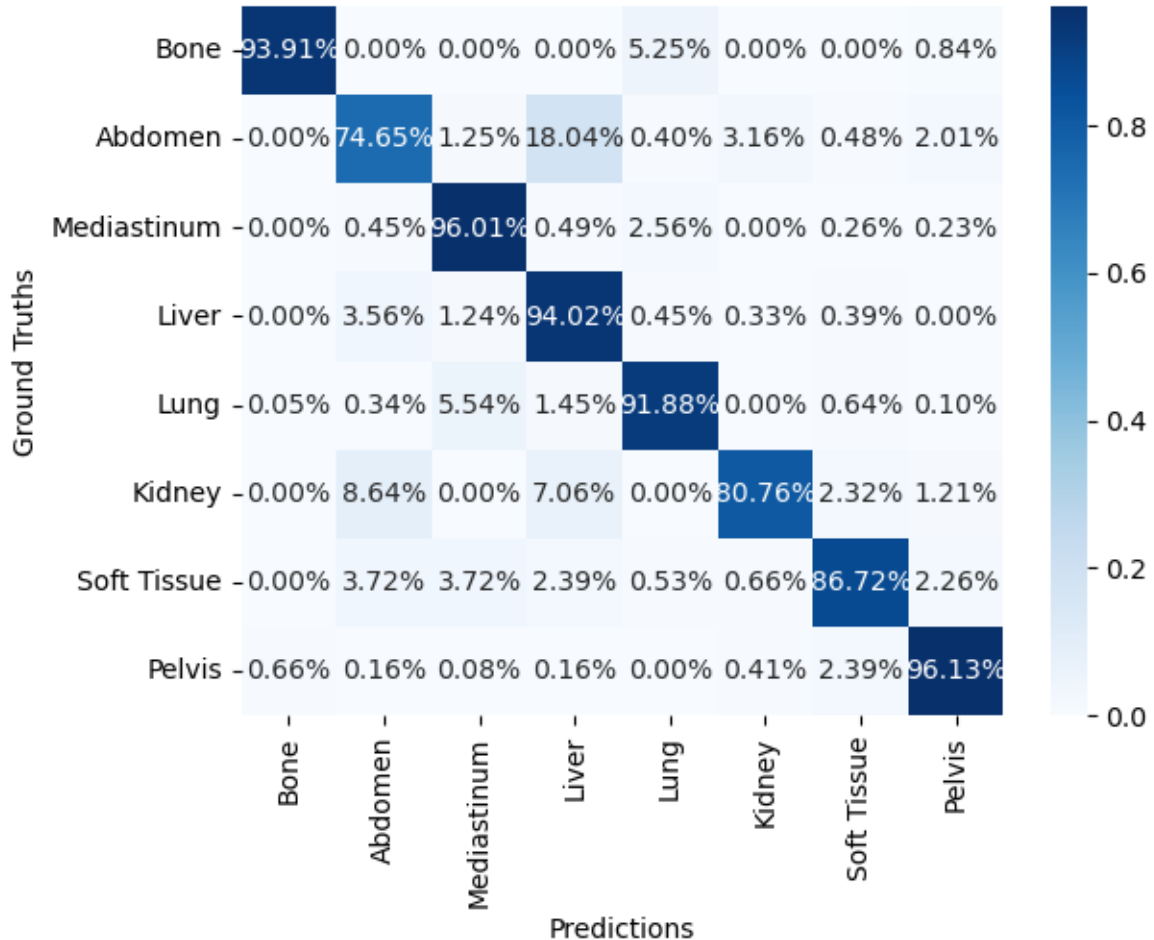


Figure 2: Normalized Confusion Matrix: No Self-Training (Baseline).

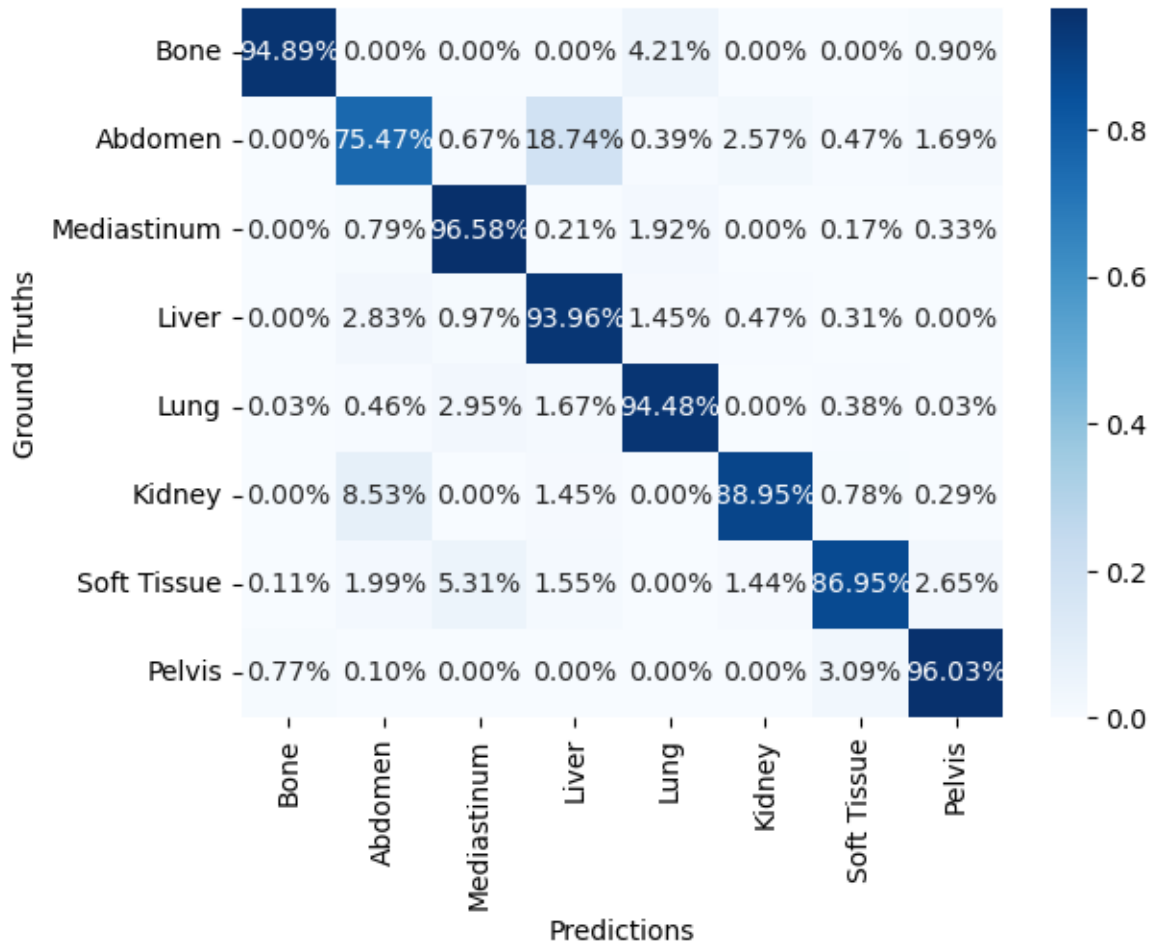


Figure 3: Normalized Confusion Matrix: Ensemble of Static Threshold Models.

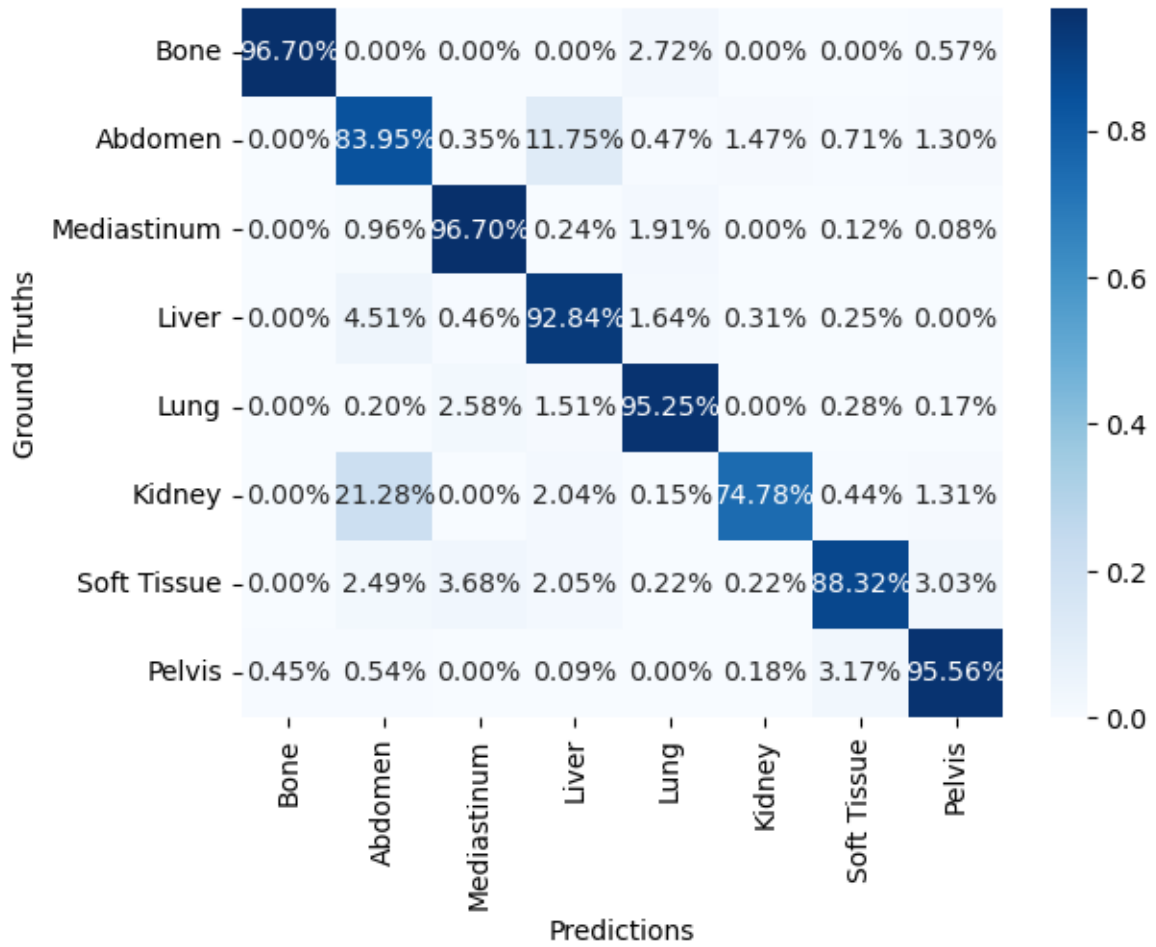


Figure 4: Normalized Confusion Matrix: Ensemble of Variable Threshold Models.